Analytical equivalent circuits for three-dimensional metamaterials and metagratings

Antonio Alex-Amor◎,[1,*] Salvador Moreno-Rodríguez◎,[2] Pablo Padilla◎,[2]
Juan F. Valenzuela-Valdés◎,[2] and Carlos Molero◎[2]

[1]*Department of Information Technology, Universidad San Pablo-CEU, CEU Universities, Campus Montepríncipe,
28668 Boadilla del Monte, Madrid, Spain*

[2]*Department of Signal Theory, Telematics and Communications, Research Centre for Information and
Communication Technologies (CITIC-UGR), University of Granada, 18071 Granada, Spain*

Recently, three-dimensional (3D) metamaterials have undergone a revolution driven mainly by the popularization of 3D-printing techniques, which has enabled the implementation of modern microwave and photonic devices with advanced functionalities. However, the analysis of 3D metamaterials is complex and computationally costly in comparison with the analysis of their one-dimensional and two-dimensional counterparts due to the intricate geometries involved. In this paper, we present a fully analytical framework based on Floquet-Bloch modal expansions of the electromagnetic fields and integral-equation methods for the analysis of 3D metamaterials and metagratings. Concretely, we focus on 3D configurations formed by periodic arrangements of rectangular waveguides with longitudinal slot insertions. The analytical framework is computationally efficient compared with full-wave solutions and also works under oblique-incidence conditions. Furthermore, it comes associated with an equivalent circuit that allows one to gain physical insight into the scattering and diffraction phenomena. The analytical equivalent circuit is tested against full-wave simulations in CST. Simulation results show that the proposed 3D structures provide independent polarization control of the two orthogonal polarization states. This key property is of potential interest for the production of full-metal polarizers, such as the one illustrated here.

I. INTRODUCTION

Modern analog microwave and photonic devices, such as frequency-selective surfaces, waveguide devices, filters, absorbers, antennas, or polarizers, are based on the use of metamaterials [1–8]. Metamaterials are artificially engineered devices that allow arbitrary control and manipulation of the propagation of electromagnetic waves [9,10]. Traditionally, metamaterials have comprised periodic or quasiperiodic arrangements of subwavelength insertions, i.e., structures whose constituent elements repeat periodically in space [11], time [12], or space-time [13,14]. Historically, scientific and engineering communities have paid special attention to one-dimensional (1D) and two-dimensional (2D) metamaterial configurations due to the simplicity related to their analysis, design, and manufacturing [15]. Nonetheless, 1D and 2D metamaterials have fundamental limitations inherent to their geometry, such as independent orthogonal polarization control [16]. These limitations are mainly due to the fact that 1D and 2D

configurations do not exploit the degrees of freedom associated with the longitudinal direction, the spatial direction in which the wave actually propagates. In that sense, three-dimensional (3D) metamaterials are required to overcome the limitations of 1D and 2D configurations [17], leading to a new era in the metamaterial field from which wireless communication systems can benefit.

The popularization of 3D metamaterials is recent. At the cost of increasing the cell thickness, a new degree of freedom is introduced, which can be used to improve the performance of the device. This is associated with the exploitation of the longitudinal direction (*z* direction) in the design. The different homogeneous longitudinal sections, i.e., waveguide regions, can be modified by the insertion of longitudinal slots. The inclusion of longitudinal slots allow the electromagnetic response of the 3D device to be tuned in an effective manner, with potential application in reflectarray and transmitarray technology and other microwave and photonic devices [16,17]. For instance, this inclusion often increases angular stability, allows dual-band frequency responses, increases the operational bandwidth, and provides structural robustness. This should be considered a valuable asset not present

---

*Corresponding author: antonio.alexamor@ceu.es

in flat 2D metasurfaces or in stacks of 2D devices (2.5D metastructures).

For the aforementioned reasons, 3D metamaterials are starting to be applied in microwave and photonics engineering for the realization of advanced polarizers [18], absorbers [19], beam-forming systems [20], and wide-angle impedance-matching layers [21] and to control orthogonal linear polarizations in reflectarray and transmitarray cells [22]. This has been made possible thanks to the evolution of 3D-printing techniques and the impressive increase in computational resources in recent years [16,17,23–25]. Nonetheless, 3D metamaterials are bulkier than flat devices and, usually, more difficult to analyze due to their complex geometry. Robust and generalist full-wave tools, such as the finite-elements method or finite-difference time-domain techniques [26], can be used for the analysis of 3D metamaterials. Normally, the use of the previously mentioned methods comes at the cost of great computational resources and a lack of physical insight into the electromagnetic behavior of the structure. Some more-efficient and more-physically-insightful alternatives to full-wave methods were discussed in Ref. [16], among which homogenization theory [27,28], modal analysis [29, 30], ray optics [31,32], transfer-matrix analysis [33,34], circuit models [35,36], or some specific combination of these can be found.

Among the methods mentioned above, circuit models are of particular interest. Complex physical phenomena can be described in a straightforward manner with the use of equivalent circuits ruled by basic circuit theory and its main components: voltage and current sources, impedances, admittances, and transmission lines [37,38]. Furthermore, circuit models are remarkably more computationally efficient than other numerical techniques. Without loss of generality, we can classify equivalent circuits into two main types: (i) heuristic and (ii) analytical. Heuristic approaches need the support of an external method or simulator, such as CST STUDIO or Ansys HFSS, to calculate the value of their circuit components. There are many examples in the literature where heuristic equivalent circuits were used to model and characterize complex electromagnetic phenomena in metamaterials and frequency-selective-surface structures [39–43]. On the other hand, analytical circuit approaches do not need external support, i.e. they are fully operational by themselves [44–48]. This fact constitutes a major difference between heuristic and analytical equivalent circuits. Nevertheless, analytical circuit models are often restricted to canonical geometries since complex geometries may not be easily modeled with analytical mathematical expressions.

In this paper, we propose a rigorous and systematic analytical framework based on integral-equation techniques and Floquet-Bloch series expansions of the electromagnetic fields to analyze 3D metamaterials and metagratings. Related formulations have been successfully applied for the analysis of 1D [49–52] and 2D [44,53–56] metamaterial structures and, more recently, to time-varying systems [57–59]. Similarly to previous approaches, the analytical formulation is connected to an *analytical equivalent circuit* that models the 3D structure.

In all cases, we are dealing with thick (nonflat) metamaterials with a 3D profile, formed by 2D-periodic arrangements of slotted waveguides (SWGs). The insertion of longitudinal slots modifies the electromagnetic response of the 3D metastructure, allowing us to control and manipulate the transmission and reflection of electromagnetic waves. The proposed 3D metastructures are fundamentally based on metallic waveguide geometries. Thus, their interior is essentially hollow, filled with air. This reduces the weight of the structure, since the volume of metal or metallized material is small compared with the total volume of the metadevice.

The equivalent circuit is constituted by lumped elements that describe higher-order wave coupling between the different waveguide sections, and transmission lines that characterize the wave propagation in the different regions. To the best of our knowledge, this is one the first times that a rigorous fully analytical equivalent circuit is proposed to model a 3D metamaterial. Some of the previous approaches found in the literature have purely heuristic [21,35,60] or quasiheuristic (mixture of heuristic and analytical) [61] rationales, but none is purely analytical. Fully analytical schemes are preferred over heuristic or quasiheuristic ones, as they are independent of external full-wave simulations. Thus, the present analytical equivalent circuit can be used as an efficient surrogate model and can be combined with artificial-intelligence or conventional optimization techniques for the design of 3D devices.

All of the structures considered are of fully metallic nature. Nonetheless, the inclusion of dielectrics in the hollow waveguide sections can be easily treated from an analytical perspective with the circuit approach, if necessary. There are many commercial applications where fully metallic structures are preferred over dielectric ones. For instance, the use of dielectrics is not recommended in space applications, as the thermal-expansion coefficients of dielectrics differ from those of metals, resulting in an uneven, nonuniform volume expansion, which can lead to structure failure. In general, fully metallic structures fit very well in scenarios where systems are subjected to large thermal variations, both in space and on Earth. Additionally, the use of fully metallic configurations, such as the ones presented in this work, is beneficial for operation at high frequencies. This is motivated by two main reasons. Firstly, dielectrics increase structure losses significantly as the frequency increases. Fully metallic structures are much more robust with regard to losses, as Ohmic losses are much easier to control provided that proper fabrication processes are applied. Secondly, fully metallic designs

can be easily scaled in frequency compared with mixed metallodielectric or fully dielectric designs.

The paper is organized as follows. The derivation of the analytical equivalent circuit that models 3D metamaterials is presneted in Sec. II. Then, some numerical computations are performed to check the correct operation of the circuit approach, including for reflective and transmitting structures. A relation between the original 3D metagrating and advanced configurations is shown in Sec. III. It is shown that, in certain circumstances, related advanced configurations can be also analyzed with the present approach. The use of the present circuit model for the efficient design of polarizer devices is detailed in Sec. IV. Finally, some general conclusions obtained from the work are presented in Sec. V.

II. THEORETICAL FRAMEWORK AND RESULTS

The original metamaterial considered is illustrated in Fig. 1(a). It is a thick 3D metastructure formed by a 2D-periodic arrangement (periodicities p_x and p_y along the x and y directions, respectively) of metallic waveguides with slot insertions placed along the longitudinal direction z. The unit cell of the 3D metamaterial is highlighted in blue and the main geometrical parameters are indicated. The corresponding unit cell is bounded by periodic boundary conditions in the x and y directions.

The 3D metagrating (with 2D periodicity) shown in Fig. 1 shares some similarities with multilayer devices formed by stacks of 2D metasurfaces (commonly named "2.5D structures"), especially from an analytical perspective. In 2.5D structures, each (meta)layer that form the stack is homogenized and modeled as a shunt impedance or admittance, while the connecting homogeneous media between layers (typically air or generic dielectrics) are modeled as transmission lines [55,56]. A similar approach is followed here for the analysis of the proposed 3D metadevice. The transitions between different waveguide sections are modeled as shunt admittances, while the connecting media (homogeneous waveguides) are modeled as transmission lines. Although the applied rationale could seem to be rather similar in both the 2.5D case and the 3D case, the homogeneous waveguide sections discussed here are significantly more complex to describe analytically, as are the transitions between them. More importantly, the main difference between a 2.5D device (multilayer stack) and the proposed 3D device lies in the fact that in a multilayer stack the longitudinal direction cannot be exploited from a design perspective. This is not the case in the 3D device shown here, where the homogeneous waveguide sections can be modified by the insertion of longitudinal slots, which allows us to control and manipulate in a more-efficient manner the transmission and reflection of electromagnetic waves.

Thus, the longitudinal structure of the cell can be split into several homogeneous regions: on the one hand, regions where there are no perforations, emulating conventional metallic rectangular waveguides (RWGs) with dimensions $w_x \times w_y$; on the other hand, regions where perforations exist, emulating homogeneous *hard waveguides* (HWGs) with dimensions $p_x \times h_1$ or $p_x \times h_2$, and where the TEM mode can propagate. As the cross-section view in Fig. 1(b) shows, HWG regions are stretched along the y axis. In general, HWGs can be regarded as parallel-plate waveguides whose lateral walls are periodic boundary conditions. When normal incidence is considered, the symmetry of the cell with respect to the principal planes reduces the periodic boundary conditions on the walls to perfect-magnetic-conductor (PMC) or perfect-electric-conductor (PEC) conditions. For an incident electric field vector polarized along $\hat{\mathbf{y}}$ (according to the frame of coordinates in Fig. 1), periodic boundary conditions in the Y-Z plane become PMC conditions. This situation is the most interesting since slot resonators may exhibit their resonant conditions. We henceforth focus on this scenario.

The equivalent circuit that describes the physical phenomenology associated with the 3D metagrating is illustrated in Fig. 1(c). Each discontinuity is modeled as a shunt equivalent admittance that takes into account all relevant information about higher-order coupling between evanescent modes/harmonics. For the present 3D structure, we have three main discontinuities, labeled as I, II, and III. Discontinuity I models the transition between the input medium (typically considered here to be air) and the RWG. Discontinuity II models the transition between the RWG and the lowest hard waveguide (RWG-HWG transition). Discontinuity III models the transition between the lowest and highest hard waveguides (HWG-HWG transition). Discontinuities IV, V, and VI are of the same type as discontinuities III, II, and I, respectively. This is discussed later in more detail. Finally, each waveguide section (rectangular and hard) is circuitally modeled as a transmission line of length d_i, with specific values of the characteristic admittance and propagation constant (they depend on the waveguide nature). It is always assumed that the propagation is performed by the fundamental mode/harmonic of each of the regions. Input and output media are semi-infinite spaces characterized by semi-infinite transmission lines with characteristic admittance $Y_{00}^{(in)}$ and $Y_{00}^{(out)}$, respectively.

Circuit parameters will be dependent on the geometry of the 3D structure. As explained below, the admittances associated with the rest of the transmission lines (and other shunt admittances participating in the equivalent circuit in Fig. 1) are multiplied by a factor of α_i, denoting the degree of coupling at the discontinuity planes. This factor is circuitally interpreted as a transformer with turn ratio $1:\sqrt{\alpha_i}$, as explicitly shown, for example, in Refs. [52,62].
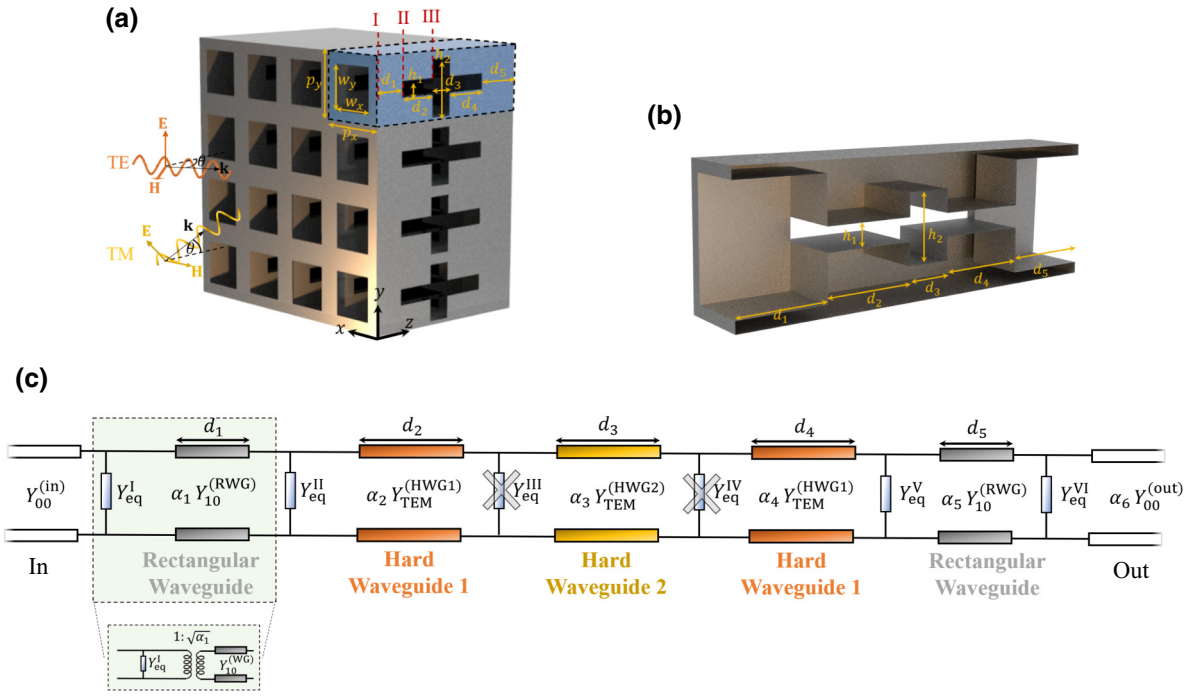
FIG. 1. (a) Three-dimensional metamaterial formed by periodic repetitions of rectangular waveguides with longitudinal cross-shaped slot insertions. The unit cell of the 3D structure is highlighted in blue. (b) Cross-section view of a unit cell. (c) Analytical Floquet equivalent circuit.

The current circuit version sketched in Fig. 1(c) is equally valid and is selected to reduce the matrix-formalism complexity when different transmission-line sections are being cascaded (see the Appendix).

As reported in Refs. [18,61], slots in the *Y*-*Z* plane are easily excitable by $\hat{\mathbf{y}}$-polarized waves, and exhibit no effects for the opposite polarization. An identical rationale can be used for resonators on the *X*-*Z* plane and $\hat{\mathbf{x}}$-polarized incident waves. We henceforth focus on cells with resonators on the *Y*-*Z* plane and fed by $\hat{\mathbf{y}}$-polarized plane waves. The conclusions obtained are valid for the resonators on the *X*-*Z* plane fed by $\hat{\mathbf{x}}$-polarized incident electric fields.

A. Input-medium–waveguide discontinuity (I)

For the derivation of the circuit parameters, we consider the case of a plane wave having the transverse electric field vector oriented towards $\hat{\mathbf{y}}$. This scenario can be covered by TM- (E_y, E_z, H_x) and TE- (E_y, H_x, H_z) polarized plane waves impinging obliquely (angle θ), as illustrated in Fig. 1(a). Time-harmonic variation ($e^{j\omega t}$) is present in all the electromagnetic fields considered and thus is suppressed from now on.

The characterization of the discontinuity departs from the knowledge, *a priori*, of the electromagnetic field expansion at both sides of the discontinuity. In the input

region, referenced by the superscript "(in)," the transverse electric field can be expressed by a Floquet series of harmonics. Each of these harmonics is excited after the interaction of the incident wave and the discontinuity.

Assuming TM incidence, the field expansion in the air region can be written at the discontinuity plane ($z = 0$) as follows [53,55]:

$$
\begin{aligned}
&\mathbf{E}^{(\mathrm{in})}(x,y) \\
&= \frac{1}{\sqrt{p_x p_y}}(1 + E_{00}^{\mathrm{TM,(in)}})e^{-jk_t y}\hat{\mathbf{y}} \\
&\quad + \frac{1}{\sqrt{p_x p_y}}\sum_{\forall n,m \neq 0,0} E_{nm}^{\mathrm{TE,(in)}}\frac{k_m\hat{\mathbf{x}} - k_n\hat{\mathbf{y}}}{k_{nm}}e^{-j(k_n x + k_m y)} \\
&\quad + \frac{1}{\sqrt{p_x p_y}}\sum_{\forall n,m \neq 0,0} E_{nm}^{\mathrm{TM,(in)}}\frac{k_n\hat{\mathbf{x}} + k_m\hat{\mathbf{y}}}{k_{nm}}e^{-j(k_n x + k_m y)}, \quad (1)
\end{aligned}
$$

with the unity being the normalized amplitude of the incident wave and $E_{00}^{\mathrm{TM,(in)}}$ the unknown reflection coefficient. The coefficients $E_{nm}^{\mathrm{TE,(in)}}$ and $E_{nm}^{\mathrm{TM,(in)}}$ are the unknown amplitudes associated with TE/TM nm harmonics. The transverse wavevector of an nmth harmonic is referred to as k_{nm}, defined as

$$
k_{nm} = \sqrt{k_n^2 + k_m^2}, \quad (2)
$$

with

$$k_n = \frac{2\pi n}{p_x}, \tag{3}$$

$$k_m = \frac{2\pi m}{p_y} + k_t. \tag{4}$$

The longitudinal component of the wavevector of an nm harmonic is denoted by β_{nm}:

$$\beta_{nm} = \sqrt{k_0^2 - k_{nm}^2}, \tag{5}$$

with $k_0 = \omega/c$.

Similarly, the magnetic field expansion may be expressed as follows [53,55]:

$$
\begin{aligned}
\mathbf{H}^{(\text{in})}(x,y) \\
= & -\frac{Y_{00}^{\text{TM},(\text{in})}}{\sqrt{p_x p_y}} (1 - E_{00}^{\text{TM},(\text{in})}) e^{-jk_t y} \hat{\mathbf{y}} \\
& - \frac{1}{\sqrt{p_x p_y}} \sum_{\forall n,m \neq 0,0} Y_{nm}^{\text{TE},(\text{in})} E_{nm}^{\text{TE},(\text{in})} \frac{k_m \hat{\mathbf{y}} + k_n \hat{\mathbf{x}}}{k_{nm}} e^{-j(k_n x + k_m y)} \\
& - \frac{1}{\sqrt{p_x p_y}} \sum_{\forall n,m \neq 0,0} Y_{nm}^{\text{TM},(\text{in})} E_{nm}^{\text{TM},(\text{in})} \frac{k_n \hat{\mathbf{y}} - k_m \hat{\mathbf{x}}}{k_{nm}} e^{-j(k_n x + k_m y)},
\end{aligned}
\tag{6}
$$

with

$$Y_{nm}^{\text{TE},(\text{in})} = \frac{\beta_{nm}^{(\text{in})}}{\eta_0 k_0}, \tag{7}$$

$$Y_{nm}^{\text{TM},(\text{in})} = \frac{k_0}{\eta_0 \beta_{nm}^{(\text{in})}} \tag{8}$$

being the nmth-order TE and TM admittances, respectively, where η_0 is the free-space impedance.

In the RWG region, the field expansion is written in terms of the modal solutions of the RWG. However, in frequency ranges far below the excitation of higher-order modes, the electromagnetic field description inside the RWG may be represented in terms of a single mode—say, the fundamental TE_{10} mode:

$$\mathbf{E}^{(\text{RWG})}(x,y) = E_{10}^{\text{TE},(\text{RWG})} \frac{2}{\sqrt{2}} \frac{1}{\sqrt{w_x w_y}} \cos(k_{10}^{(\text{RWG})} x) \hat{\mathbf{y}}, \tag{9}$$

$$\mathbf{H}^{(\text{RWG})}(x,y) = Y_{10}^{\text{TE},(\text{RWG})} [\mathbf{E}^{(\text{RWG})}(x,y) \cdot \hat{\mathbf{y}}] \hat{\mathbf{x}}, \tag{10}$$

with $E_{10}^{\text{TE},(\text{RWG})}$ the unknown amplitude of the TE_{10} mode, $k_{10}^{(\text{RWG})} = \pi/w_x$, and $Y_{10}^{\text{TE},(\text{RWG})} = \beta_{10}^{(\text{RWG})}/\eta_0 k_0$. The propagation constant $\beta_{10}^{(\text{RWG})}$ is similarly obtained as in Eq. (5), by replacement of k_{nm} by $k_{10}^{(\text{RWG})}$.

The analytical derivation of the equivalent circuit requires an *a priori* estimation of the field profile at the discontinuity. Given the geometry considered, the field profile (spatial distribution) is expected to be similar to the fundamental or TE_{10} mode at lower frequencies. Thus, the field at the discontinuity may be described as

$$\mathbf{E}_{\text{dis}} = A \cos\left(\frac{\pi}{w_x} x\right) \hat{\mathbf{y}}, \tag{11}$$

where A is a frequency-dependent constant to be determined. This estimation is good enough for frequencies below the onset of higher-order modes inside the RWG. For normal incidence, the second mode excitable is the TE_{30} mode, whose cutoff frequency $f_{30} = 3f_{10}$, with $f_{10} = ck_{10}^{(\text{RWG})}/2\pi$ being the cutoff frequency of the TE_{10} mode.

The analytical expressions for the unknown amplitudes of each of the modes/harmonics in both regions are obtained after imposition of the following conditions at the discontinuity:

$$\mathbf{E}^{(\text{in})}(x,y) = \mathbf{E}_{\text{dis}}, \tag{12}$$

$$\mathbf{E}^{(\text{RWG})}(x,y) = \mathbf{E}_{\text{dis}}, \tag{13}$$

$$\mathbf{E}_{\text{dis}} \times [\mathbf{H}^{(\text{in})}(x,y)]^* = \mathbf{E}_{\text{dis}} \times [\mathbf{H}^{(\text{RWG})}(x,y)]^*, \tag{14}$$

where Eqs. (12) and (13) refer to the continuity of the electric field and Eq. (14) describes the continuity of the Poynting vector.

By developing the above equations after introducing the harmonic/modal expansion inside, and after several mathematical calculations, we obtain the following expression for the reflection coefficient $E_{00}^{\text{TM},(\text{in})}$:

$$E_{00}^{\text{TM},(\text{in})} = \frac{Y_{00}^{(\text{in})} - \alpha_{10}^{\text{TE},(\text{RWG})} Y_{10}^{\text{TE},(\text{RWG})} - Y_{\text{eq}}^{\text{I}}}{Y_{00}^{(\text{in})} + \alpha_{10}^{\text{TE},(\text{RWG})} Y_{10}^{\text{TE},(\text{RWG})} + Y_{\text{eq}}^{\text{I}}}, \tag{15}$$

with

$$Y_{\text{eq}}^{\text{I}} = \sum_{\forall n,m \neq 0,0} \left[\alpha_{nm}^{\text{TE},(\text{in})} Y_{nm}^{\text{TE},(\text{in})} + \alpha_{nm}^{\text{TM},(\text{in})} Y_{nm}^{\text{TM},(\text{in})} \right]. \tag{16}$$

The factors $\alpha_{nm}^{\text{TE},(\text{in})}$, $\alpha_{nm}^{\text{TM},(\text{in})}$, and $\alpha_{10}^{\text{TE},(\text{RWG})}$ represent the coupling among all the harmonics/modes and $\mathbf{E}_{\text{dis}}$, whose expressions are given by

$$\alpha_{nm}^{\text{TE},(\text{in})} = \left[\pi^2 \frac{k_n}{k_{nm}} \frac{\cos(k_n w_x/2)}{(k_n w_x)^2 - \pi^2} \frac{\sin(k_m w_y/2)}{\sin(k_t w_y/2)} \frac{k_t}{k_m} \right]^2, \tag{17}$$

$$\alpha_{nm}^{\text{TM},(\text{in})} = \frac{k_m^2}{k_n^2} \alpha_{nm}^{\text{TE},(\text{in})}, \tag{18}$$

$$\alpha_{10}^{\text{TE},(\text{RWG})} = \frac{\pi^2}{8} \frac{p_x p_y}{w_x w_y} \left[\frac{k_t w_y/2}{\sin(k_t w_y/2)} \right]^2. \tag{19}$$

The above expressions and the reflection-coefficient equation (15) lead to the identification of a transmission-line model where $Y_{00}^{(\text{in})}$ and $\alpha_{10}^{\text{TE,(RWG)}} Y_{10}^{\text{TE,(RWG)}}$ are the characteristic admittances of the input and output transmission lines in discontinuity I, respectively. They are formally the transmission lines in white and gray in the equivalent circuit in Fig. 1. Henceforth, the parameter multiplying the admittance of the TE_{10} mode is redefined as follows:

$$\alpha_1 = \alpha_{10}^{\text{TE,(RWG)}}. \tag{20}$$

The admittance Y_{eq}^{I} is the shunt admittance connecting both transmission lines.

A similar derivation can be done for TE incidence. In this case the transverse electric field vector points towards $\hat{\mathbf{y}}$ (this plane wave is completed by magnetic field components pointing towards $\hat{\mathbf{x}}$ and $\hat{\mathbf{z}}$). The rationale used is identical, but some of the expressions must now be redefined. Equations (21) and (22) are rewritten as

$$k_n = \frac{2\pi n}{p_x} + k_t, \tag{21}$$

$$k_m = \frac{2\pi m}{p_y} \tag{22}$$

since the transverse component of the wavevector is pointing towards $\hat{\mathbf{x}}$, as mentioned above.

Furthermore, by applying the same method, we achieve the following expressions for the factors multiplying the TE and TM admittances in Y_{eq}^{I}:

$$\alpha_{nm}^{\text{TE,(in)}}$$
$$= \left[\frac{k_n}{k_{nm}} \frac{\cos(k_n w_x/2)}{\cos(k_t w_x/2)} \frac{(k_t w_x)^2 - \pi^2}{(k_n w_x)^2 - \pi^2} \frac{\sin(k_m w_y/2)}{k_m w_y/2} \right]^2, \tag{23}$$

$$\alpha_{nm}^{\text{TM,(in)}} = \frac{k_m^2}{k_n^2} \alpha_{nm}^{\text{TE,(in)}}, \tag{24}$$

$$\alpha_{10}^{\text{TE,(RWG)}} = \frac{1}{8\pi^2} \frac{p_x p_y}{w_x w_x} \left[\frac{(k_t w_x)^2 - \pi^2}{\cos(k_t w_x/2)} \right]^2, \tag{25}$$

which contribute to redefining the admittances occurring in the equivalent circuit. The factor associated with the TE_{10} mode, α_1, is the same as in Eq. (20).

B. Rectangular-waveguide–hard-waveguide discontinuity (II)

To model discontinuity II, we assume the RWG is the input medium and the HWG with dimensions $p_x \times h_1$ is the output medium. That is, the *feeding port* is set on the RWG side. In Sec. II A, it was assumed that the TE_{10} mode was the dominant field inside the RWG (both in the evanescent

state and in the propagative state). This approximation is valid for frequencies below and above the cutoff frequency of this mode, and it is also applied in this section. Thus, the *incident field* is now the TE_{10} mode of the RWG.

The interaction of this mode with the discontinuity excites all the possible modal solutions in both waveguides. In the RWG region, the TE_{10} mode is highly dominant and thus the modal expansion is exactly the same as that in Eqs. (9) and (10). In the HWG, the excitable modal solutions *under the incidence* of the TE_{10} mode are those that respect the same symmetric conditions imposed by this mode. After some mathematical and physical analysis, it can be concluded that modal solutions with even orders n and m can be excited only at the discontinuity. The electric field expansion in the HWG region therefore may be described as

$$\mathbf{E}^{(\text{HWG})}(x, y) = \frac{1}{\sqrt{p_x w_y}} E_{00}^{(\text{HWG})} \hat{\mathbf{y}}$$

$$+ \left[\sum_{\substack{\forall n > 0 \\ \forall m \geq 0}} \gamma_{nm}^{(\text{HWG})} E_{nm}^{\text{TE,(HWG)}} k_n^{(\text{HWG})} \right.$$

$$\left. \times \cos(k_n^{(\text{HWG})} x) \cos(k_m^{(\text{HWG})} y) \right] \hat{\mathbf{y}}$$

$$- \left[\sum_{\substack{\forall n \geq 0 \\ \forall m > 0}} \gamma_{nm}^{(\text{HWG})} E_{nm}^{\text{TM,(HWG)}} k_m^{(\text{HWG})} \right.$$

$$\left. \times \cos(k_n^{(\text{HWG})} x) \cos(k_m^{(\text{HWG})} y) \right] \hat{\mathbf{y}} \tag{26}$$

for n and m even numbers and with

$$\gamma_{n0}^{(\text{HWG})} = \frac{2}{\sqrt{2}} \frac{1}{k_n^{(\text{HWG})}} \frac{1}{\sqrt{p_x w_y}}, \tag{27}$$

$$\gamma_{0m}^{(\text{HWG})} = \frac{2}{\sqrt{2}} \frac{1}{k_m^{(\text{HWG})}} \frac{1}{\sqrt{p_x w_y}}, \tag{28}$$

$$\gamma_{nm}^{(\text{HWG})} = \frac{1}{2} \frac{1}{k_{nm}^{(\text{HWG})}} \frac{1}{\sqrt{p_x w_y}}, \tag{29}$$

$$k_n^{(\text{HWG})} = \frac{n\pi}{p_x} \qquad \forall n \text{ even}, \tag{30}$$

$$k_m^{(\text{HWG})} = \frac{m\pi}{h_1} \qquad \forall m \text{ even}. \tag{31}$$

The field profile at the discontinuity is that used in Sec. II A, specified in Eq. (11). Taking this into account, and imposing similar continuity conditions as Eqs. (12)–(14), we obtain the expression for an equivalent admittance for discontinuity II that includes the effect of

all the higher-order harmonics in the HWG:

$$Y_{\text{eq}}^{\text{II}} = \sum_{\substack{\forall n>0 \\ \forall m \geq 0}} \alpha_{nm}^{\text{TE,(HWG)}} Y_{nm}^{\text{TE,(HWG)}}$$

$$+ \sum_{\substack{\forall n \geq 0 \\ \forall m>0}} \alpha_{nm}^{\text{TM,(HWG)}} Y_{nm}^{\text{TM,(HWG)}}, \qquad (32)$$

where the factors α can be defined as

$$\alpha_1 \alpha_{n0}^{\text{TE,(HWG)}} = 32\pi^2 \frac{w_x w_y}{p_x h_1} \left[\frac{\cos(k_n^{\text{(HWG)}} w_x/2)}{(k_n^{\text{(HWG)}} w_x)^2 - \pi^2} \right]^2, \quad (33)$$

$$\alpha_1 \alpha_{nm}^{\text{TE,(HWG)}}$$
$$= 64\pi^2 \frac{w_x w_y}{p_x h_1}$$
$$\times \left[\frac{k_n^{\text{(HWG)}}}{k_{nm}^{\text{(HWG)}}} \frac{\cos(k_n^{\text{(HWG)}} w_x/2)}{(k_n^{\text{(HWG)}} w_x)^2 - \pi^2} \frac{\sin(k_m^{\text{(HWG)}} w_y/2)}{k_m^{\text{(HWG)}} w_y/2} \right]^2,$$
$$(34)$$

$$\alpha_1 \alpha_{0m}^{\text{TM,(HWG)}} = \frac{32}{\pi^2} \frac{w_x w_y}{p_x h_1} \left[\frac{\sin(k_m^{\text{(HWG)}} w_y/2)}{k_m^{\text{(HWG)}} w_y/2} \right]^2, \quad (35)$$

$$\alpha_{nm}^{\text{TM,(HWG)}} = \left[\frac{k_m^{\text{(HWG)}}}{k_{nm}^{\text{(HWG)}}} \right]^2 \alpha_{nm}^{\text{TE,(HWG)}}. \qquad (36)$$

The parameter α_1 is as defined in Eq. (20). The admittance $Y_{\text{eq}}^{\text{II}}$ is connected to the input and output transmission lines in gray and orange in Fig. 1. They are the input and output lines of this discontinuity, corresponding to the TE_{10} and TEM modes, respectively. The characteristic admittances are given by $\alpha_1 Y_{10}^{\text{TE,(RWG)}}$ and $\alpha_2 Y_{\text{TEM}}^{\text{(HWG1)}}$, with

$$\alpha_1 \alpha_2 = \frac{16}{\pi^2} \frac{w_x w_y}{p_x h_1} \qquad (37)$$

and $Y_{\text{TEM}}^{\text{(HWG1)}} = 1/\eta_0$.

C. Hard-waveguide–hard-waveguide discontinuity (III)

To model this kind of discontinuity, we take into account the previous conclusions obtained from the other discontinuity types. Now, two different HWGs are in contact at the discontinuity. The input HWG, being the output region in the previous section, has dimensions $p_x \times h_1$. The output HWG has dimensions $p_x \times h_2$. The feeding mode is now the TEM mode coming from the input HWG. At the discontinuity, the field at both sides is expressed as in

Eq. (26), but with use of the correct dimensions (p_x and h_1 for the input region, and p_x and h_2 for the output region) in the wave numbers k_n and k_m.

The field profile at the discontinuity is proportional to the TEM mode in the lowest-height HWG:

$$\mathbf{E}_d = A\hat{\mathbf{y}}. \qquad (38)$$

Assuming $h_1 < h_2$, and applying again the boundary conditions in Eqs. (12)–(14), we obtain

$$E_{nm}^{\text{TE/TM,(HWG1/HWG2)}} = 0 \quad \text{if } n \neq 0 \text{ or } m \neq 0, \qquad (39)$$

indicating that no higher-order modes are considered under this approximation. This approximation works well up to the excitation of the first higher-order mode. Therefore, the fundamental modes (TEM modes) of each of the waveguides are represented by transmission lines with characteristic admittances $Y_{\text{TEM}}^{\text{(HWG1)}} = Y_{\text{TEM}}^{\text{(HWG2)}} = 1/\eta_0$, being the transmission lines in orange and yellow, respectively, in Fig. 1. The parameter α_3 is defined as follows:

$$\alpha_1 \alpha_2 \alpha_3 = \frac{h_1}{h_2}. \qquad (40)$$

It is worth remarking that in case that $h_1 > h_2$, Eq. (40) becomes

$$\alpha_1 \alpha_2 \alpha_3 = \frac{h_2}{h_1}. \qquad (41)$$

In a first approach, the shunt admittance connecting both transmission lines can be ignored, $Y_{\text{eq}}^{\text{III}} = 0$, since it is formally formed by all the higher modes $E_{nm}^{\text{TE/TM,(HWG1)/(HWG2)}}$, which are not excited under the conditions imposed at the discontinuity according to Eq. (39). This constitutes an approximation, which is expected to work well up to the excitation of the higher-order modes in any of the HWGs.

D. Numerical examples: reflective structures

We now present some numerical results to validate and test the capabilities of the analytical equivalent circuit. We initially consider the 3D metamaterial structure included as an inset in Fig. 2(a), with its associated circuit shown in Fig. 2(d). It is a fully metallic device, short-circuited at its end, that operates as a reflective structure. From the circuit point of view, the input admittance seen from discontinuity III through the short-circuited line can be represented as

$$Y_{\text{in}}^{\text{(HWG2)}} = -j \alpha_3 Y_{\text{TEM}}^{\text{(HWG2)}} \cot(k_0 d_3). \qquad (42)$$

The longitudinal cross-shaped slots and the associated waveguide stretches allow one to control the phase of the reflected wave in an efficient manner.
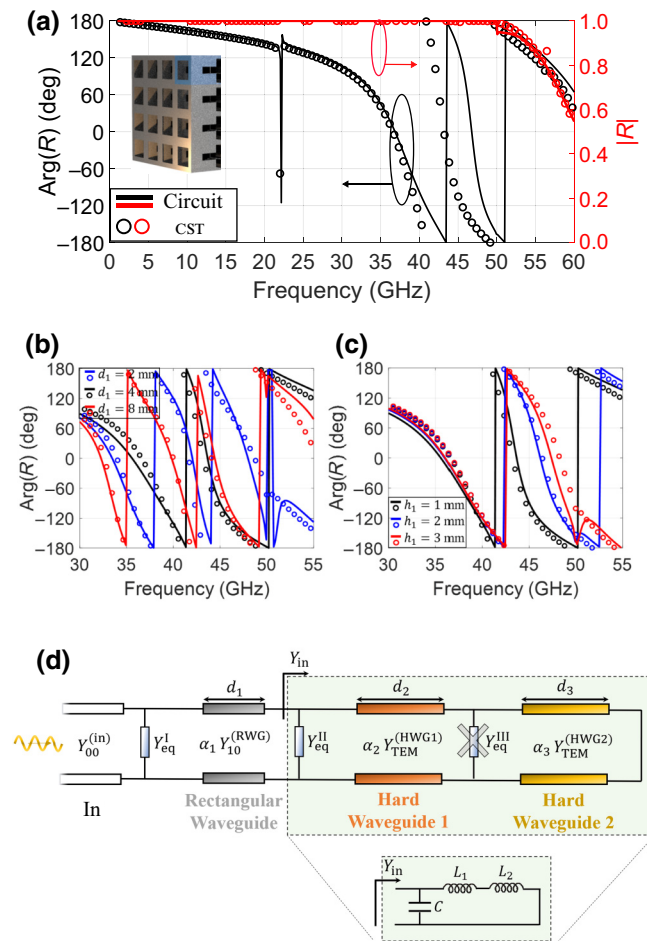
FIG. 2. Reflection coefficient R of a reflective 3D structure for $d_1 = 4$ mm and $h_1 = 1$ mm. (a) Phase and amplitude. (b) Effect of varying d_1. (c) Effect of varying h_1. In all cases, solid colored lines and colored circles correspond to the analytical and full-wave results, respectively. (d) Analytical circuit model. Geometrical parameters $p_x = p_y = 6$ mm, $w_x = w_y = 5$ mm, $d_2 = 4$ mm, $d_3 = 0.5$ mm, and $h_2 = 3$ mm. Normal incidence.

Figure 2(a) provides a comparison between results obtained by our approach (solid lines) and by the full-wave simulator CST STUDIO (circles). The parameters computed are the phase (black) and amplitude (red) of the reflection coefficient R. As observed, there is good agreement between the analytical and full-wave-simulator results over a wide range of frequencies. For the dimensions of the unit cell (6×6 mm^2), the onset frequency of the first higher-order harmonic is 50 GHz for normal incidence. Naturally, the computation time for the analytical circuit (order of seconds) is much less than that of CST (order of minutes or hours could be needed). For 1001 frequency points, the circuit approach took less than 2 second to give the solution, while CST took more than 400 second in the simplest case.

The cutoff frequency of the square-waveguide section is 30 GHz for the selected dimensions (5×5 mm^2). This

implies that only evanescent modes are excited inside the 3D metagrating below 30 GHz. Nonetheless, in cases where the RWG length is short enough, modes of evanescent nature in the RWG (e.g., TE$_{10}^{(\mathrm{RWG})}$) may couple to the HWG section. This is due to the *slow* decay rate of the amplitude of the TE$_{10}$ mode along the short RWG section. The HWG is therefore excited by the evanescent TE$_{10}$ mode, manifested by the propagation of its fundamental mode, now identified as a propagating TEM mode. This excitation via evanescent waveguides is analogous to the well-known tunnel effect in quantum physics [63], and is particularly relevant to design transmitting structures via opaque waveguides. Such is the case described in Sec. II E.

The spectral evolution of the reflection coefficient plotted in Fig. 2(a) exhibits a rich phenomenology, especially for frequencies higher than 30 GHz. However, a sudden resonance jump appears at around 22 GHz, identified as a sudden $\lambda/2$ resonance in the HWG regions. The total length of the two HWG sections (transmission-line sections) $D = d_2 + d_3 = 4.5$ mm. The corresponding $\lambda/2$ resonance would be expected at 33.3 GHz if the HWGs were isolated. However, the HWGs sections are coupled to a RWG section, whose common discontinuity junction is modeled by the admittance $Y_{\mathrm{eq}}^{\mathrm{II}}$, predominantly capacitive. The presence of this capacitance is responsible for the resonance shifting to lower frequencies, in this case down to 22 GHz. The rest of the RWG section contributes as an inductive load, although its influence over the rest of the structure is not very relevant. The phase evolution starts to vary faster beyond 30 GHz, frequency at which the TE$_{10}$ mode becomes propagative. Both the $\lambda/4$ peak and this fast evolution of the phase at higher frequencies are well captured by the equivalent circuit, since it predicts all this phenomenology.

In Fig. 2(a), the red curve and circles show the amplitude evolution of the reflection coefficient. As expected, the reflective character of the cell invokes full reflection up to 50 GHz. Above 50 GHz, the first higher-order harmonic in the air region becomes propagative, and thus the reflected power is split in two: part is carried by the incident wave and part is carried by the higher-order harmonic. This is the reason why the reflection coefficient represented in Fig. 2(a) is no longer one beyond 50 GHz. Again, this phenomenon is well captured by the equivalent circuit.

Figures 2(b) and 2(c) illustrate the spectral evolution of the reflection phase when some geometrical parameters of the structure are modified. As expected, the increase of the lengths of the RWG and HWG sections has a direct impact on the phase response of the system. Figure 2(b) shows the phase modification when the length of the RWG section d_1 is varied. A comparison is made between the analytical circuit results (solid lines) and the CST results (circles), showing very good agreement in all cases. Slight differences can be appreciated at high frequencies, due to the complexity of the structure. Moreover, the model

seems to be more accurate for larger values of d_1. For $d_1 = 2$ mm, differences between the CST approach and the circuit approach can be appreciated at lower frequencies in comparison with cases with higher values of d_1. The reason for this disagreement is related to the lack of information associated with higher-order modes inside the RWG. The model assumes the excitation of the TE_{10} mode (both of evanescent nature and of propagative nature nature), and avoids the excitation of the rest of the higher-order modes. When d_1 is large and the TE_{10} mode is evanescent (under 30 GHz), its amplitude decays along the RWG and it does not reach the end of the RWG. As d_1 decreases, this amplitude may not decay along the RWG length and the modal field can reach the end of the waveguide, coupling to the next waveguide (HWG). For $d_1 \ll \lambda$, the TE_{10} mode does arrive at the end, but neither do some of the higher-order modes that have not been taken into account. When the frequency is higher than 30 GHz, the TE_{10} mode becomes propagative and its amplitude stops decaying. The model captures well this fact. However, the presence of the other higher-order modes is not considered in the circuit model, and thus a lack of accuracy is expected when $d_1 \ll \lambda$. As can be appreciated from Fig. 2(b), this disagreement from 30 GHz is not visible for $d_1 = 4$ and $d_1 = 8$ mm.

Figure 2(c) shows the phase variation when h_1 is modified. The smaller h_1 is, the greater the observed phase shift is. Physical insight into this phenomenon can be achieved by means of the analytical circuit model. For HWGs with short lengths ($d_2, d_3 \ll \lambda$), the short-circuited HWG sections contribute to the circuit model with a pure inductive term $L = L_1 + L_2$. In addition, the equivalent admittance that models the RWG-HWG discontinuity, Y_{eq}^{II}, contributes with a pure capacitive term C at frequencies above the RWG cutoff. Thus, the RWG-HWG-short section, whose input admittance is Y_{in} [see Fig. 2(d)], can be simply described as an LC tank. Decrease of the height of the HWG results in its lower and upper metallic plates being closer. As a consequence, the associated capacitance C increases, shifting down in frequency the position of the curves in Fig. 2(c). Note that this effect is not appreciable near the cutoff of the square waveguide (30 GHz for the selected geometry), as the capacitive term C is not dominant yet.

Finally, results considering oblique incidence are plotted in Fig. 3. TE and TM incidences are included, manifested by the incidence of a plane wave with incidence angle $\theta = 15°$. The results provided by the circuit model fit well with those obtained by CST up to 40 GHz approximately. Beyond this frequency, the agreement notably deteriorates, due to the excitation of additional modes that are not included in the analytical circuit derivation. Specially, higher-order modes inside the RWG are now determinant, as the TE_{11} mode, with cutoff frequency $f_{11} = 42.43$ GHz. Since this mode is excluded from the circuit derivation, the degradation manifested in Fig. 3 near and beyond f_{11} is
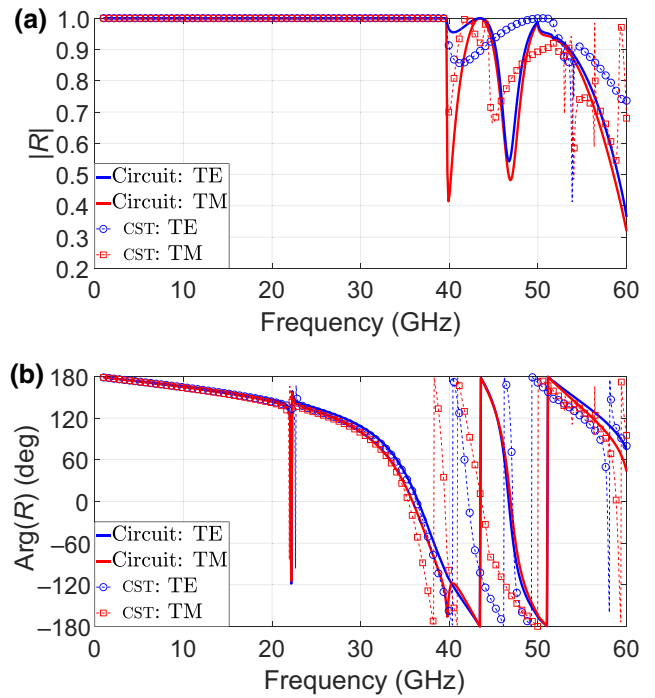

FIG. 3. Reflection coefficient R of a reflective 3D structure under oblique-incidence conditions ($\theta = 15°$). (a) Amplitude. (b) Phase. Geometrical parameters $p_x = p_y = 6$ mm, $w_x = w_y = 5$ mm, $d_1 = d_2 = 4$ mm, $d_3 = 0.5$ mm, $h_1 = 1$ mm, and $h_2 = 3$ mm.

expected. Although it constitutes an important limitation of our approach, the model is still wideband, exhibiting good performance for cell dimensions larger than $\lambda/2$. It is worth remarking that all the physical phenomena below f_{11} are well captured, as the resonance in the phase around 22 GHz.

E. Numerical examples: transmitting structures

The proposed 3D metastructure can operate in reflection and transmission modes. By minor modifications of the geometry of the waveguides that form the 3D metastructure, a design initially proposed for reflection operation can be converted into one with transmission operation. From a practical point of view, this is an interesting feature of the proposed 3D structure. When we normally consider other types of structure, specific designs are made for reflection and transmission, which can sometimes be very different from each other. In transmission mode, the 3D device can control both the amplitude and the phase of the scattered waves by properly adjustment of the geometrical parameters of rectangular and hard waveguides.

Figure 4 shows the transmission coefficient T (phase and amplitude) in the 3D transmitting structure. The performance of the analytical equivalent circuit is tested against full-wave results obtained with CST. Good agreement is
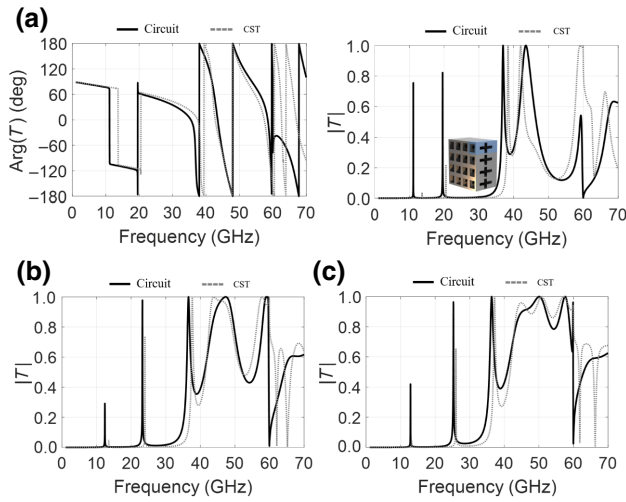
FIG. 4.   (a) Transmission coefficient T (phase and amplitude) of a transmitting 3D structure ($h_1 = 1$ mm). (b) $|T|$ for $h_1 = 2$ mm. (c) $|T|$ for $h_1 = 3$ mm. The analytical circuit model corresponds to that shown in Fig. 1(c). Geometrical parameters $p_x = p_y = 5$ mm, $w_x = w_y = 4$ mm, $d_1 = 4$ mm, $d_2 = 4$ mm, $d_3 = 1$ mm, $d_4 = 4$ mm, $d_5 = 4$ mm, and $h_2 = 3$ mm. Normal incidence is assumed.

FIG. 5.   Amplitude of the reflection coefficient of a reflective 3D structure. Copolarization (E_{xx}, E_{yy}) and cross-polarization (E_{xy}, E_{yx}) terms are plotted. Geometrical parameters $p_x = p_y = 6$ mm, $w_x = w_y = 5$ mm, $d_1 = 4$ mm, $d_2 = 6$ mm, $h_x = 1$ mm, and $h_y = 2$ mm.

generally observed in a wideband range. For the calculation of 5001 frequency points, the circuit approach took less than 4 seconds, while CST took more than 10 min. Time-domain full-wave solvers such as CST are highly dependent on the size of the structure being analyzed. Transmitting structures are longer than reflective structures, so computation times notably increase. Remarkably, our circuit approach is, for all practical purposes, independent of the size considered. Even-odd excitation techniques [45,62] can be considered for the analysis of longitudinally symmetric transmitting structures such as the one considered here (symmetric with respect to the plane $Z = d_1 + d_2 + d_3/2$), approximately halving the computation time.

In Fig. 4, two resonant transmission peaks appear below the cutoff frequency of the RWG (37.5 GHz for the selected geometry). As previously discussed, evanescent waves travel along the RWG and, at some particular frequencies, may couple to the HWG sections, led by the fundamental TEM mode. Thus, narrowband transmission occurs below the cutoff of the RWG. The two narrowband transmission peaks are caused by $\lambda/2$ and λ resonances in the HWG sections. Ideally, for the selected length of the HWG sections (9 mm in total), the $\lambda/2$ resonance would be located at 16.67 GHz if the HWG sections were isolated from the RWG and uniform in height. In practice, Figs. 4(a)–4(c) show that the $\lambda/2$ resonance is located at 11.2, 12.4, and 13 GHz, respectively, for increasing height h_1. As the height of the HWG increases, the simulated resonance approaches the theoretical estimation, as the capacitive contribution
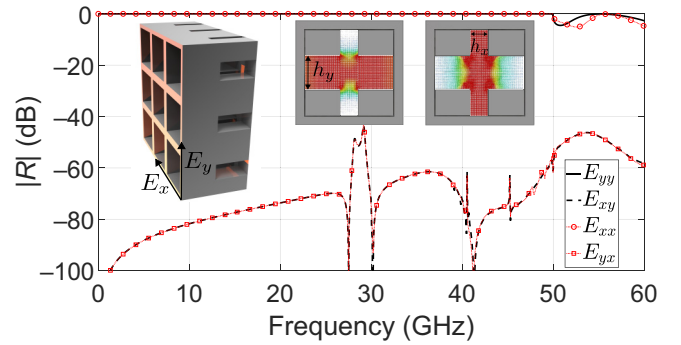
of Y_{eq}^{II} and Y_{eq}^{V} (RWG-HWG transitions) is less prominent. The same rationale holds for the λ resonance created by the HWG.

The circuit approach stops being accurate beyond 60 GHz. This coincides with the onset of the first higher-order mode in the HWG, at 60 GHz (larger dimension/periodicity $p_x = 5$ mm). In any case, the accuracy of the model is quite good below this frequency, covering a large bandwidth.

F. Independent polarization control

Another interesting property of the proposed 3D metamaterial is the independent polarization control of its two orthogonal linear states (X and Y polarizations). This is a key feature that can be exploited for the efficient design of polarizer devices. Independent polarization control is possible thanks to the use of the longitudinal direction as an additional degree of freedom. As shown in Refs. [18,61], resonators perforated on the waveguide walls in the X-Z plane control X polarization and are opaque for Y polarization. The opposite situation is achieved when the resonators are perforated on the Y-Z wall. Specific 2D metasurface designs may achieve a certain degree of polarization independence [64,65]; however, this independence is highly sensitive to the scatterer shape and geometry. In 3D architectures, the resonator shapes do not break the polarization-independence property. Focusing on the structure under consideration in the present paper, one can easily achieve independent polarization control by placing an additional perpendicular HWG section. Thus, the HWG section in the 3D structure is now stretched along the x and y directions, as the insets in Fig. 5 illustrate.

In Fig. 5, the orthogonal polarization independence is tested in a reflective structure (short-circuited at its end). Figure 5 shows the amplitude of the reflection coefficient R for two perpendicular polarizations at normal incidence.

In the legend, E_{ij} ($i,j = \{x,y\}$) represents the electric field associated with input i-polarized (horizontal) and output j-polarized (vertical) waves. Thus, subindexes ii and jj represent the copolarization terms, while ij and ji represent the cross-polarization terms. The cross-polarization level is less than -40 dB in a wideband range. Therefore, a great polarization independence can be claimed for the horizontal and vertical polarizations. Note that from 50 GHz onwards, the single-mode behavior of the structure ceases as the second mode of the HWG becomes propagative, as do the first-orders harmonics in the air region.

For a visual representation, the inset in Fig. 5 depicts the electric field profile of the fundamental mode for the horizontal and vertical polarizations. The electric field profile was obtained by full-wave simulations in CST. When the incident wave is polarized along the y axis, the entire electric field is confined within the horizontal HWG. Cutting of the structure at the center part does not significantly affect the electric field pattern, which still shows a TEM-like profile. This fact leads to the low cross-polarization coupling level evidenced in Fig. 5. The scenario is identical for an x-polarized incident wave. Most of the electric field is confined in the vertical HWG, also leading to a TEM-like profile. Polarization independence can be advantageously used for the design of polarizer devices, by simply tuning the length of the vertical and horizontal slots. Thus, a $0°$-phase or $180°$-phase resonance can be achieved when the length of the short-circuited slot is $\lambda/4$ or $\lambda/2$, respectively [60].

In addition, the polarization independence is also advantageous from the circuital point of view, since an individual and independent circuit approach can be used for the control of each of the polarizations (x and y). The global problem, involving both polarizations, is split into two independent subproblems (one for the x component and one for the y component).

III. RELATED 3D STRUCTURES

In this section, we show that the proposed analytical circuit approach can be used not only for the analysis of the original 3D device shown in Fig. 1 but also for the characterization of related 3D metastructures and metagratings. As we show, in some circumstances, related 3D structures exhibit electromagnetic behavior similar to that of the originally proposed 3D metamaterial, and thus the analytical equivalent circuit is still applicable.

Specifically, we focus on the alternative version of the original 3D metamaterial shown in Fig. 6. The alternative structure is similar in all aspects to the original one, except for the waveguide sections where the longitudinal slots are inserted. In the alternative 3D structure (Fig. 6), the upper and lower metallic walls are not stretched along the y direction in the slotted waveguide (SWG) region. This leads to a different field excitation in the SWG [66].
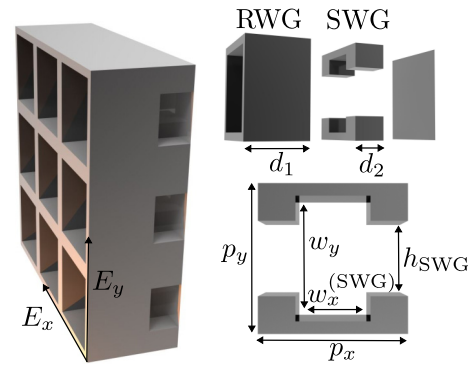

FIG. 6. "Alternative" 3D metamaterial formed by RWG and SWG sections. Note that its internal structure differs from that of the "original" 3D metamaterial (RWG and HWG sections) shown in Fig. 1(a). Geometrical parameters $p_x = p_y = 6$ mm, $w_x = w_y = 5$ mm, $w_x^{(\mathrm{SWG})} = 3$ mm, $d_1 = 4$ mm, and $d_2 = 6$ mm. w_y is identical for the RWG and SWG regions.

In general, electromagnetic fields within the SWG region are different and of more-complex nature than for a HWG. Note that a HWG is bounded with PEC conditions at the upper and lower walls and PMC conditions at the lateral walls, which simply excites a TEM mode at low frequencies. The situation is different in a SWG section, where the electric field profile shows a TEM-like profile within the slotted region but does not vanish outside this region. However, in certain circumstances, it can be demonstrated that the SWG can behave effectively as a HWG, i.e., $\mathbf{E}^{(\mathrm{HWG})} \approx \mathbf{E}^{(\mathrm{SWG})}$. In those cases, the original and alternative 3D metastructures will show similar electromagnetic responses and, therefore, both can be analyzed with the analytical equivalent circuit. This scenario is illustrated in Fig. 7. The reflection coefficient R is plotted for the original (solid lines) and alternative (dashed lines) 3D structures versus the height of the longitudinal slots.

Figures 7(a) and 7(b) present scenarios where wide and narrow longitudinal slots are considered, respectively. The results suggest that wide slots in the SWG ($h_{\mathrm{SWG}} \gtrsim 0.6 w_y$) lead to similar electromagnetic responses between the original and alternative 3D metastructures. This is observed for a wide range of frequencies. On the other hand, the frequency range where the original and alternative 3D structures show similar electromagnetic behavior significantly reduces when narrow slots ($h_{\mathrm{SWG}} \lesssim 0.6 w_y$) are inserted. This can be qualitatively explained by looking at the electric field profiles of the HWG and SWG shown in Fig. 7. The electric field must vanish at the upper and lower metallic walls in the SWG region. In the extreme case $h_{\mathrm{SWG}} = w_y$, the SWG section transforms into an actual HWG governed by the fundamental TEM mode. For this extreme case, the electromagnetic response of the original 3D structure and the electromagnetic response of the alternative 3D structure are indistinguishable.

FIG. 8.   Line impedance in the SWG and HWG as a function of the height h. Geometrical parameters $p_x = p_y = 6$ mm, and $w_x^{(\mathrm{SWG})} = 3$ mm. Results obtained with CST STUDIO.
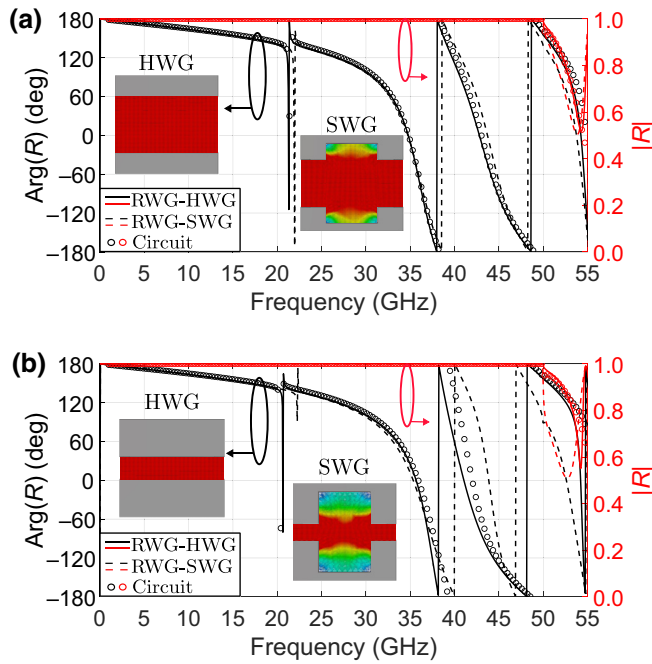
FIG. 7.   Comparison of the phase of the reflection coefficient for two different reflective metastructures: original (RWG and HWG sections) and alternative (RWG and SWG sections). Solid and dashed colored lines correspond to full-wave results, while colored circles correspond to analytical results. The height of the slotted regions is varied. (a) $h_{\mathrm{SWG}} = 3$ mm, $h_{\mathrm{HWG}} = 3.42$ mm. (b) $h_{\mathrm{SWG}} = 1$ mm, $h_{\mathrm{HWG}} = 1.375$ mm. The original and alternative 3D structures show similar electromagnetic responses when the slot height is large [(a)]. Geometrical parameters $p_x = p_y = 6$ mm, $w_x = 5$ mm, $w_y = 5$ mm, $w_x^{(\mathrm{SWG})} = 3$ mm, $d_1 = 4$ mm, and $d_2 = 6$ mm.

As the slot becomes progressively narrower (h_{SWG} decreases), differences between both configurations start to appear, mainly at high frequencies. In cases where the slot is wide [Fig. 7(a)], the electric field in the SWG is mainly of TEM nature, as the edge of the slot is close to the upper and lower metallic walls. From a practical perspective, the complex SWG can be reduced to an equivalent HWG section for operation. The equivalent HWG would be of same width (p_x) as the SWG and effective height h_{eff}. The concept of *effective height* is heuristically introduced after inspection of the excited fields in the SWG. It can be observed that the electric field is fundamentally confined in the slot (h_{SWG}) plus a tiny vertical region Δh_{SWG}, and thus $h_{\mathrm{eff}} = h_{\mathrm{SWG}} + \Delta h_{\mathrm{SWG}}$. By analysis of the SWG in the alternative 3D structure as an equivalent HWG, the circuit model is able to provide accurate results for the scattering phenomena, as Fig. 7(a) illustrates.

The situation is not so simple when narrow SWG slot insertions ($h_{\mathrm{SWG}} \lesssim 0.6 w_y$) are considered. In this case, as Fig. 7(b) illustrates, the excited fields in the SWG depart from the TEM profile seen in the HWG. This
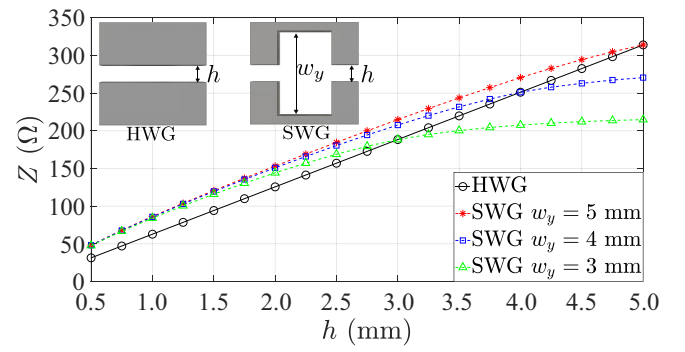
fact becomes especially noticeable at high frequencies, where the original (solid lines) and alternative (dashed lines) 3D structures no longer show similar electromagnetic responses. Consequently, as discussed at the end of Sec. II E, the results obtained with the circuit approach (circles) and CST (solid line) slightly differ from each other when narrow slots are considered. This is due to the intense capacitive effects introduced by $Y_{\mathrm{eq}}^{\mathrm{II}}$ in the HWG, thus leading to the resonant frequency obtained by CST (38.16 GHz) being somewhat lower than that calculated by the circuit approach (39.26 GHz). The distance between the top and bottom walls at the center of the SWG region (set by w_y) results in the capacitance of the SWG being smaller than that of the HWG.

To estimate the effective height h_{eff}, Fig. 8 depicts the line impedance at 30 GHz of the HWG and SWG structures. Note that the line impedance is plotted as a function of the height of the slot (h). These results were obtained from port information in CST (version 2022). It is worth noting that Z is the impedance associated with the propagative TEM mode through the uniform line. In the SWG, these curves were obtained for three different values of w_y: 3 mm (dashed green line), 4 mm (dashed blue line), and 5 mm (dashed red line).

Naturally, when the values of w_y and h are identical in the SWG structure, the impedance obtained coincides with that of the HWG. As a result, the impedance curves cross each other. However, the impedance values that are of particular interest in this work are those above the HWG curve (solid black line). In these cases, the original and alternative 3D structures are expected to show similar electromagnetic responses and, therefore, both can be analyzed with the present analytical circuit approach. Thus, it can be seen that for any selected height of the SWG, there is another (greater) effective height of the HWG where their impedances coincide. As an example, a SWG region with $h = 3$ mm and $w_y = 5$ mm will have the same line impedance (at 30 GHz) as a HWG region with $h_{\mathrm{eff}} = 3.42$ mm.

IV. APPLICATIONS: FULL-METAL POLARIZER

One of the main advantages of the proposed 3D metamaterials is the independent control of the two orthogonal polarization states. This became evident after evaluation of the results presented in Figs. 5 and 7. Independent polarization control is a remarkable feature, rarely found in 1D and 2D implementations, that can be advantageously exploited for the design and prototyping of full-metal polarizers.

As an example, the proposed analytical approach is applied for the design of a reflective polarizer that operates from 35 to 43.2 GHz. The proposed 3D device rotates the polarization plane of the reflected wave by 90° in the selected frequency range. Consequently, the direction of rotation of a circularly polarized incident wave will also change. This is one of the main applications in which the analytical circuit study can be used from an engineering perspective. It is worth noting that the purpose of this section is not to design a state-of-the-art polarizer but to show the applicability of the circuit approach in real-world scenarios.

Figure 9(a) shows a sketch of the fully metallic 3D reflective polarizer. As can be appreciated, the 3D polarizer is composed of all the regions described above: RWG, SWG, and HWG. Note that with this configuration it is possible to achieve slots of different lengths in the vertical and horizontal walls, and thus the resonances can be tuned by modification of d_2 and d_3.

Reflective fully metallic 3D structures allow simple but efficient polarizer designs due to the low Ohmic losses involved. As the polarizers are short-circuited at the end of the structures, only the phase shift between the orthogonal components of the incident electric field needs to be set for the design of polarizers of different nature. To polarize an incoming wave whose electric field vibrates along the $\hat{\mathbf{u}}$ direction [shown in Fig. 9(a)], it is sufficient to set the phases separately from the reflection coefficient R of its main components E_x and E_y. Therefore, if the reflection coefficient of E_x and E_y in their copolarization direction (E_{xx} and E_{yy}) has a phase shift of 180°, a rotator is achieved. From a design perspective, it is common to assume a maximum error of $(180 \pm 37)°$ [67,68]. This error band fixes the operation bandwidth of the polarization rotator.

The operation of the polarizator rotator is as follows. For the E_{xx} and E_{yy} components, the incident wave impinges on the RWG section, whose dimensions prevent the propagation of the fundamental mode below 30 GHz. Subsequently, the propagative $\mathrm{TE}_{10}^{(\mathrm{RWG})}$ mode is guided from 30 to 50 GHz by the SWG and the short-circuited HWG as a TEM-like mode and a TEM mode, respectively. Thus, single-mode operation is guaranteed from 30 to 50 GHz. Above 50 GHz, the amplitude decays as the second propagative mode is excited. A center frequency of 37.4 GHz is assumed as a starting design point. At this frequency, the
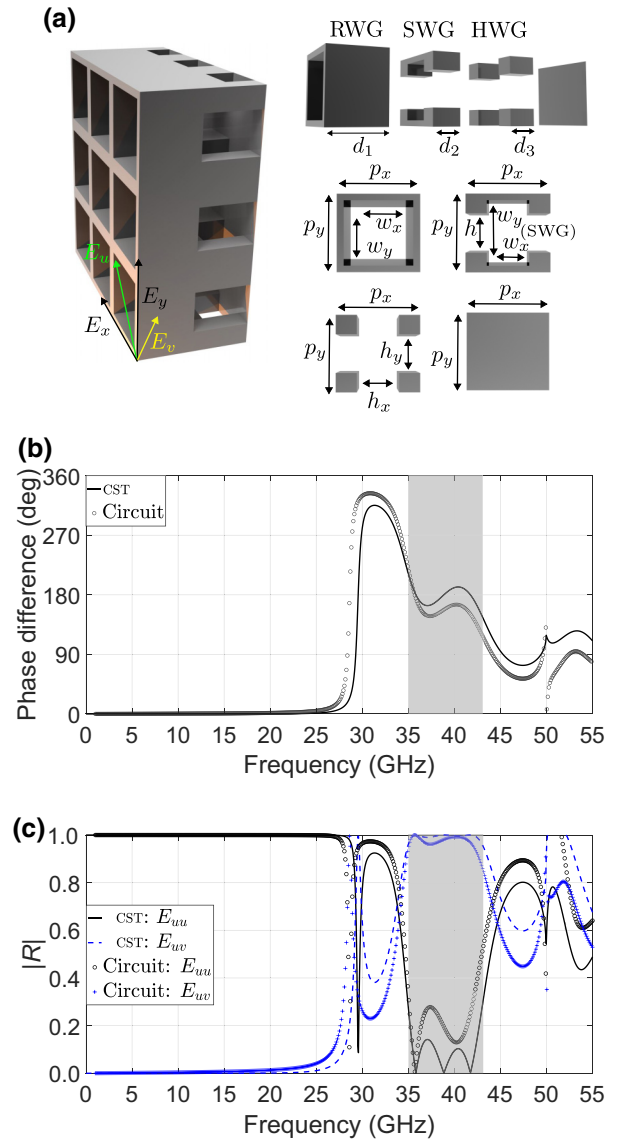

FIG. 9. (a) A 3D reflective polarization rotator. (b) Phase difference between the reflection coefficient of the vertical copolarization (E_{yy}) and the reflection coefficient of the horizontal copolarization (E_{xx}). (c) Amplitude of the reflection coefficient R, showing the copolarization (black) and cross-polarization (blue) components for E_u and E_v. The shadowed region (in gray) indicates the operative range of the polarization rotator. Solid and dashed lines correspond to full-wave results, and circles and crosses correspond to analytical results. Geometrical parameters $p_x = p_y = 6$ mm, $w_x = w_y = 5$ mm, $w_x^{(\mathrm{SWG})} = 3$ mm, $d_1 = 4$ mm, $d_2 = d_3 = 2$ mm, $h = 3$ mm, and $h_x = h_y = 3$ mm.

shorter vertical slot insertion (SWG-HWG-short section) creates a $\lambda/4$ resonance, while the larger horizontal slot insertion (HWG-short section) creates a $\lambda/2$ resonance. The $\lambda/4$ and $\lambda/2$ resonances both produce a relative phase shift of 180° between the horizontal and vertical components, which leads to a rotation of the polarization plane

for the reflected wave. The study realized in Sec. III has made it possible to simulate the SWG region as a HWG with parameters that approximate their electromagnetic responses.

Figure 9(b) illustrates the phase difference of the reflection coefficient R of the two orthogonal components E_{xx} and E_{yy}. The shadowed region indicates the simulated bandwidth where the 3D polarization rotator is operative. In Fig. 9(c), the rotation of the electric field is directly visualized. It shows the amplitude of the reflection coefficient R for an incident wave whose electric field vibrates according to E_u. The shadowed region sets the previous bandwidth where the copolarization reflection coefficient is below to -10 dB on a logarithmic scale. Consequently, the power is transmitted to the orthogonal component E_v. As can be seen, the bandwidth obtained by the circuit model is slightly lower than the simulated bandwidth. Despite this, good agreement is observed between the full-wave numerical results obtained with CST and the analytical circuit results taking into account the variations from the original structure shown in Fig. 1. Naturally, it is important to note the difference in computational times between CST and the circuit in the design stage, beyond the physical insight that the circuit may also provide. For the extraction of the two orthogonal components, CST took approximately 10 min and the analytical circuit tool only 2 s.

It is interesting to highlight the reduced weight of the 3D polarizer. As the polarizer is based on the use of periodic waveguides (RWG, HWG, and SWG), the interior of the structure is essentially hollow and filled with air. This causes the weight of the structure to be much less than originally suspected, since the volume of metal (or metallized material) is small compared with the total volume. Of the total volume of the polarizer, approximately 63% is air, while only 37% is metal. This leads to a reduced weight of the polarizer, as well as for the other 3D metastructures presented in this work, which is of great interest for potential commercial applications.

Additionally, the proposed 3D polarizer is smaller than one may initially think. The dimensions of its unit cell are $0.75\lambda \times 0.75\lambda \times \lambda$ (width times height times thickness), considering a central frequency of 37.5 GHz. A fabricated functional polarizer would require, at least, a structure formed by 10×10 unit cells so the real-world finite implementation can be approached as periodic and analyzed with the present mathematical framework. Thus, the dimensions of the fabricated finite structure would be $7.5\lambda \times 7.5\lambda \times \lambda$. If we compare these dimensions with those required in a lens-type antenna or with other reflectarrays and transmitarrays based on 2D configurations, we see that the 3D polarizer has a relatively compact size. A compact size is a great practical advantage when one is fabricating and using 3D metastructures, e.g., for integration into mobile communication platforms.

V. CONCLUSION

Analytical modeling of complex 3D metastructures has been elusive due to the intricate geometries involved. In this paper, we have derived an analytical framework for the analysis of 3D metamaterials formed by periodic arrangements of rectangular waveguides with longitudinal slot insertions. The proposed approach comes with an associated analytical equivalent circuit. The analytical circuit model is constituted by transmission lines that model wave propagation through the different homogeneous waveguide sections and shunt equivalent admittances that model higher-order harmonic excitation at the discontinuities. It is shown that the slotted-waveguide sections can be modeled as a general waveguide with periodic boundary conditions. For the selected input excitation, and especially for normal incidence, periodic boundary conditions can be relaxed to PMC conditions. Thus, slotted-waveguide sections can be modeled as "hard waveguides." We have tested the analytical framework against full-wave numerical results. Good agreement is observed in all cases when reflective (short-circuited) and transmitting (open) 3D configurations are considered in normal-incidence and oblique-incidence conditions. In the 3D metagrating, narrowband transmission is observed at frequencies below the cutoff. In cases where the RWG is short, evanescent waves may couple to the HWG (led by its fundamental TEM mode) and may be transmitted without losses along the 3D structure. The analytical circuit model has proven to be a powerful tool to gain physical insight into complex scattering and diffraction phenomena. Additionally, the results show that the proposed 3D metamaterial is suitable for the efficient design of full-metal polarizer devices with advanced or complex functionalities. This is attributed to the reliable independent polarization control of the two orthogonal states that the 3D metamaterial exhibits. An example is the polarization rotator shown in this work, which operates from 35–44 GHz approximately. The good agreement exhibited by the full-wave and circuit results makes the circuit approach a rapid design tool. We hope that the analytical method developed in this work will be a step forward in the analysis and design of more-advanced and, surely, more-attractive 3D metastructures.

APPENDIX: TRANSMISSION MATRICES

In the way that the analytical circuit model is defined in Fig. 1(c), the computation of the scattering parameters is based on the use of transmission ($ABCD$) matrices. Shunt equivalent admittances Y_{eq} can be modeled with the following $ABCD$ matrix [69]:

$$\left[\mathbf{T}_Y(Y_{eq})\right] = \begin{bmatrix} 1 & 0 \\ Y_{eq} & 1 \end{bmatrix}. \qquad (A1)$$

Note that a short circuit in reflective structures can be modeled with the previous expression by simpling selecting $Y_{eq} \rightarrow \infty$. Waveguide sections (RWG and HWG) are modeled as lossless transmission lines according to [69]

$$\left[\mathbf{T}_L(Y_0, \beta, d)\right] = \begin{bmatrix} \cos(\beta d) & j\frac{1}{Y_0}\sin(\beta d) \\ jY_0\sin(\beta d) & \cos(\beta d) \end{bmatrix}, \qquad (A2)$$

where Y_0, β, and d are the characteristic admittance, propagation constant, and length of the transmission line.

The global transmission matrix $\left[\mathbf{T}\right]$ is computed by cascading (multiplying) the individual transmission matrices that form the complete circuit. Then the global scattering matrix $\left[\mathbf{S}\right]$ is extracted from $\left[\mathbf{T}\right]$ by use of the formulas detailed in Ref. [70], which take into consideration that the input and output media (impedance and admittance of the reference ports) could be different.

---

[1] N. Marcuvitz, *Waveguide Handbook* (McGraw-Hill, New York, NY, USA, 1951).

[2] A. Vengsarkar, P. Lemaire, J. Judkins, V. Bhatia, T. Erdogan, and J. Sipe, Long-period fiber gratings as band-rejection filters, J. Lightwave Technol. **14**, 58 (1996).

[3] P.-S. Kildal, E. Alfonso, A. Valero-Nogueira, and E. Rajo-Iglesias, Local metamaterial-based waveguides in gaps between parallel metal plates, IEEE Antennas Wirel. Propag. Lett. **8**, 84 (2009).

[4] Y. Zhao, M. A. Belkin, and A. Alú, Twisted optical metamaterials for planarized ultrathin broadband circular polarizers, Nat. Commun. **3**, 870 (2012).

[5] Y. Cui, K. H. Fung, J. Xu, H. Ma, Y. Jin, S. He, and N. X. Fang, Ultrabroadband light absorption by a sawtooth anisotropic metamaterial slab, Nano Lett. **12**, 1443 (2012). pMID: 22309161,

[6] G. Minatti, M. Faenzi, E. Martini, F. Caminita, P. De Vita, D. González-Ovejero, M. Sabbadini, and S. Maci, Modulated metasurface antennas for space: Synthesis, analysis and realizations, IEEE Trans. Antennas Propag. **63**, 1288 (2015).

[7] A. Palomares-Caballero, A. Alex-Amor, P. Padilla, and J. F. Valenzuela-Valdés, Dispersion and filtering properties of rectangular waveguides loaded with holey structures, IEEE Trans. Microw. Theory Tech. **68**, 5132 (2020).

[8] O. Quevedo-Teruel, M. Ebrahimpouri, and M. Ng Mou Kehn, Ultrawideband metasurface lenses based on off-shifted opposite layers, IEEE Antennas Wirel. Propag. Lett. **15**, 484 (2016).

[9] N. Engheta and R. Ziolkowski, *Metamaterials: Physics and Engineering Explorations* (Wiley-IEEE Press, Hoboken, NJ, USA, 2006).

[10] F. Capolino, *Theory and Phenomena of Metamaterials* (CRC Press, Boca Raton, FL, USA, 2009).

[11] D. Smith, J. B. Pendry, and M. C. K. Wiltshire, Metamaterials and negative refractive index, Science **305**, 5685 (2004).

[12] E. Galiffi, R. Tirole, S. Yin, H. Li, S. Vezzoli, P. A. Huidobro, M. G. Silveirinha, R. Sapienza, A. Alù, and J. B. Pendry, Photonics of time-varying media, Adv. Photon. **4**, 014002 (2022).

[13] C. Caloz and Z.-L. Deck-Léger, Spacetime metamaterials—part I: General concepts, IEEE Trans. Antennas Propag. **68**, 1569 (2020).

[14] S. Taravati and G. V. Eleftheriades, Generalized space-time-periodic diffraction gratings: Theory and applications, Phys. Rev. Appl. **12**, 024026 (2019).

[15] O. Quevedo-Teruel, H. Chen, A. Díaz-Rubio, G. Gok, A. Grbic, G. Minatti, E. Martini, S. Maci, G. V. Eleftheriades, and M. Chen, *et al.*, Roadmap on metasurfaces, J. Opt. **21**, 073002 (2019).

[16] A. Alex-Amor, A. Palomares-Caballero, and C. Molero, 3-D metamaterials: Trends on applied designs, computational methods and fabrication techniques, Electronics **11**, 410 (2022).

[17] M. Kadic, G. Milton, M. van Hecke, and M. Wegener, 3D metamaterials, Nat. Rev. Phys. **1**, 98 (2019).

[18] C. Molero Jimenez, E. Menargues, and M. García-Vigueras, All-metal 3-D frequency-selective surface with versatile dual-band polarization conversion, IEEE Trans. Antennas Propag. **68**, 5431 (2020).

[19] O. Tsilipakos, A. Xomalis, G. Kenanakis, M. Farsari, C. M. Soukoulis, E. N. Economou, and M. Kafesaki, Split-cube-resonator-based metamaterials for polarization-selective asymmetric perfect absorption, Sci. Rep **10**, 17653 (2020).

[20] C. Molero, A. Palomares-Caballero, A. Alex-Amor, I. Parellada-Serrano, F. Gamiz, P. Padilla, and J. F. Valenzuela-Valdés, Metamaterial-based reconfigurable intelligent surface: 3D meta-atoms controlled by graphene structures, IEEE Commun. Mag. **59**, 42 (2021).

[21] D. Bermúdez-Martín, R. Gillard, C. Molero, H. Legay, and M. García-Vigueras, Methodology for improving scanning performance loading an array element with a 3D all-metal waim, Electronics **11**, 2848 (2022).

[22] A. Palomares-Caballero, C. Molero, P. Padilla, M. García-Vigueras, and R. Gillard, Wideband 3-D-printed metal-only reflectarray for controlling orthogonal linear polarizations, IEEE Trans. Antennas Propag. **71**, 2247 (2023).

[23] H. Y. Jeong, E. Lee, S.-C. An, Y. Lim, and Y. C. Jun, 3D and 4D printing for optics and metaphotonics, Nanophotonics **9**, 1139 (2020).

[24] P. Sanchez-Olivares, M. Ferreras, E. Garcia-Marin, L. Polo-López, A. Tamayo-Domínguez, J. Córcoles, J. M. Fernández-González, J. L. Masa-Campos, J. R. Montejo-Garai, J. M. Rebollar-Machain, *et al.*, Manufacturing

guidelines for W-band full-metal waveguide devices: Selecting the most appropriate technology, IEEE Antennas Propag. Mag. **65**, 48 (2022).

[25] M. García-Vigueras, L. Polo-Lopez, C. Stoumpos, A. Dorlé, C. Molero, and R. Gillard, *Hybrid Planar*, edited by M. D. Fernandez, J. A. Ballesteros, H. Esteban, and Ángel Belenguer (IntechOpen, Rijeka, 2022) Chap. 6.

[26] T. Itoh, *Numerical Techniques for Microwave and Millimeter-Wave Passive Structures* (Wiley, Hoboken, New Jersey, USA, 1989).

[27] J. Blanchard, E. Newman, and M. Peters, Integral equation analysis of artificial media, IEEE Trans. Antennas Propag. **42**, 727 (1994).

[28] M. Silveirinha and C. Fernandes, Homogenization of 3-D-connected and nonconnected wire metamaterials, IEEE Trans. Microw. Theory Tech. **53**, 1418 (2005).

[29] O. Rabinovich and A. Epstein, Dual-polarized all-metallic metagratings for perfect anomalous reflection, Phys. Rev. Appl. **14**, 064028 (2020).

[30] N. Kari, D. Seetharamdoo, J.-M. Laheurte, and F. Sarrazin, Modal analysis of chiral metamaterial using characteristic mode analysis and eigenmode expansion method, IEEE J. Multiscale Multiphys. Comput. Tech. **5**, 37 (2020).

[31] G. Deschamps, Ray techniques in electromagnetics, Proc. IEEE **60**, 1022 (1972).

[32] Q. Liao, N. J. G. Fonseca, M. Camacho, A. Palomares-Caballero, F. Mesa, and O. Quevedo-Teruel, Ray-tracing model for generalized geodesic-lens multiple-beam antennas, IEEE Trans. Antennas Propag. **71**, 2640 (2023).

[33] Z.-Y. Li and L.-L. Lin, Photonic band structures solved by a plane-wave-based transfer-matrix method, Phys. Rev. E **67**, 046607 (2003).

[34] F. Giusti, Q. Chen, F. Mesa, M. Albani, and O. Quevedo-Teruel, Efficient Bloch analysis of general periodic structures with a linearized multimodal transfer-matrix approach, IEEE Trans. Antennas Propag. **70**, 5555 (2022).

[35] A. Grbic and G. V. Eleftheriades, An isotropic three-dimensional negative-refractive-index transmission-line metamaterial, J. Appl. Phys. **98**, 043106 (2005).

[36] M. Zedler, C. Caloz, and P. Russer, A 3-D isotropic left-handed metamaterial based on the rotated transmission-line matrix (TLM) scheme, IEEE Trans. Microw. Theory Tech. **55**, 2930 (2007).

[37] F. Mesa, R. Rodriguez-Berral, and F. Medina, Unlocking complexity using the ECA: The equivalent circuit model as an efficient and physically insightful tool for microwave engineering, IEEE Microw. Mag. **19**, 44 (2018).

[38] F. Costa, A. Monorchio, and G. Manara, Efficient analysis of frequency-selective surfaces by a simple equivalent-circuit model, IEEE Antennas Propag. Mag. **54**, 35 (2012).

[39] M. Kafesaki, I. Tsiapa, N. Katsarakis, T. Koschny, C. M. Soukoulis, and E. N. Economou, Left-handed metamaterials: The fishnet structure and its variations, Phys. Rev. B **75**, 235114 (2007).

[40] J. Carbonell, C. Croënne, F. Garet, E. Lheurette, J. L. Coutaz, and D. Lippens, Lumped elements circuit of terahertz fishnet-like arrays with composite dispersion, J. Appl. Phys. **108**, 014907 (2010).

[41] G. Perez-Palomino, J. E. Page, M. Arrebola, and J. A. Encinar, A design technique based on equivalent circuit and

coupler theory for broadband linear to circular polarization converters in reflection or transmission mode, IEEE Trans. Antennas Propag. **66**, 2428 (2018).

[42] M. Borgese and F. Costa, A simple equivalent circuit approach for anisotropic frequency-selective surfaces and metasurfaces, IEEE Trans. Antennas Propag. **68**, 7088 (2020).

[43] A. Hernández-Escobar, E. Abdo-Sánchez, P. Mateos-Ruiz, J. Esteban, T. María Martín-Guerrero, and C. Camacho-Peñalosa, An equivalent-circuit topology for lossy non-symmetric reciprocal two-ports, IEEE J. Microw. **1**, 810 (2021).

[44] R. Dubrovka, J. Vazquez, C. Parini, and D. Moore, Equivalent circuit method for analysis and synthesis of frequency selective surfaces, Proc. Inst. Elect. Eng.–Microw. Antennas Propag. **153**, 213 (2006).

[45] V. Torres, F. Mesa, M. Navarro-Cía, R. Rodríguez-Berral, M. Beruete, and F. Medina, Accurate circuit modeling of fishnet structures for negative-index-medium applications, IEEE Trans. Microw. Theory Tech. **64**, 15 (2016).

[46] A. Khavasi and B. Rejaei, Analytical modeling of graphene ribbons as optical circuit elements, IEEE J. Quantum Electron. **50**, 397 (2014).

[47] F. Mesa, R. Rodríguez-Berral, M. García-Vigueras, F. Medina, and J. R. Mosig, Simplified modal expansion to analyze frequency-selective surfaces: An equivalent circuit approach, IEEE Trans. Antennas Propag. **64**, 1106 (2016).

[48] S. Barzegar-Parizi, B. Rejaei, and A. Khavasi, Analytical circuit model for periodic arrays of graphene disks, IEEE J. Quantum Electron. **51**, 1 (2015).

[49] R. Rodriguez-Berral, F. Medina, F. Mesa, and M. Garcia-Vigueras, Quasi-analytical modeling of transmission/reflection in strip/slit gratings loaded with dielectric slabs, IEEE Trans. Microw. Theory Tech. **60**, 405 (2012).

[50] R. Rodríguez-Berral, C. Molero, F. Medina, and F. Mesa, Analytical wideband model for strip/slit gratings loaded with dielectric slabs, IEEE Trans. Microw. Theory Tech. **60**, 3908 (2012).

[51] C. Molero, R. Rodríguez-Berral, F. Mesa, and F. Medina, Analytical circuit model for 1-D periodic T-shaped corrugated surfaces, IEEE Trans. Antennas Propag. **62**, 794 (2014).

[52] C. Molero, R. Rodríguez-Berral, F. Mesa, and F. Medina, Wideband analytical equivalent circuit for coupled asymmetrical nonaligned slit arrays, Phys. Rev. E **95**, 023303 (2017).

[53] R. Rodríguez-Berral, F. Mesa, and F. Medina, Analytical multimodal network approach for 2-D arrays of planar patches/apertures embedded in a layered medium, IEEE Trans. Antennas Propag. **63**, 1969 (2015).

[54] C. Molero, M. García-Vigueras, R. Rodríguez-Berral, F. Mesa, and N. Llombart, Equivalent circuit approach for practical applications of meander-line gratings, IEEE Antennas Wirel. Propag. Lett. **16**, 3088 (2017).

[55] A. Alex-Amor, F. Mesa, A. Palomares-Caballero, C. Molero, and P. Padilla, Exploring the potential of the multi-modal equivalent circuit approach for stacks of 2-D aperture arrays, IEEE Trans. Antennas Propag. **69**, 6453 (2021).

[56] C. Molero, A. Alex-Amor, F. Mesa, A. Palomares-Caballero, and P. Padilla, Cross-polarization control in FSSs by means of an equivalent circuit approach, IEEE Access **9,** 99513 (2021).

[57] A. Alex-Amor, S. Moreno-Rodríguez, P. Padilla, J. F. Valenzuela-Valdés, and C. Molero, Diffraction phenomena in time-varying metal-based metasurfaces, Phys. Rev. Appl. **19,** 044014 (2023).

[58] S. Moreno-Rodríguez, A. Alex-Amor, P. Padilla, J. F. Valenzuela-Valdés, and C. Molero, Time-periodic metallic metamaterials defined by floquet circuits, ArXiv preprint, ArXiv:2211.13271 (2023).

[59] A. Alex-Amor, C. Molero, and M. G. Silveirinha, Analysis of metallic space-time gratings using Lorentz transformations, Phys. Rev. Appl. **20,** 014063 (2023).

[60] M. A. Balmaseda-Márquez, S. Moreno-Rodríguez, P. H. Zapata, C. Molero, and J. F. Valenzuela-Valdés, Fully-metallic 3D cells for wideband applications, IEEE Trans. Antennas Propag. **71,** 4588 (2023).

[61] C. Molero and M. García-Vigueras, Circuit modeling of 3-D cells to design versatile full-metal polarizers, IEEE Trans. Microw. Theory Tech. **67,** 1357 (2019).

[62] C. Molero, R. Rodríguez-Berral, F. Mesa, F. Medina, and A. B. Yakovlev, Wideband analytical equivalent circuit for one-dimensional periodic stacked arrays, Phys. Rev. E **93,** 013306 (2016).

[63] D. Griffiths, *Introduction to Quantum Mechanics* (Prentice Hall, Upper Saddle River, NJ, USA, 1995).

[64] S. Mercader-Pellicer, W. Tang, D. Bresciani, H. Legay, N. J. G. Fonseca, and G. Goussetis, Angularly stable linear-to-circular polarizing reflectors for multiple beam antennas, IEEE Trans. Antennas Propag. **69,** 4380 (2021).

[65] A. A. Omar, Z. Shen, and S. Y. Ho, Multiband and wideband 90° polarization rotators, IEEE Antennas Wirel. Propag. Lett. **17,** 1822 (2018).

[66] C. Molero, H. Legay, T. Pierré, and M. García-Vigueras, Broadband 3D-printed polarizer based on metallic transverse electro-magnetic unit-cells, IEEE Trans. Antennas Propag. **70,** 4632 (2022).

[67] W. Chen, C. A. Balanis, and C. R. Birtcher, Checkerboard EBG surfaces for wideband radar cross section reduction, IEEE Trans. Antennas Propag. **63,** 2636 (2015).

[68] Z. Zhang, J. Wang, X. Fu, Y. Jia, H. Chen, M. Feng, R. Zhu, and S. Qu, Single-layer metasurface for ultra-wideband polarization conversion: bandwidth extension via Fano resonance, Sci. Rep. **11,** 585 (2021).

[69] D. M. Pozar, *Microwave Engineering* (Wiley, Hoboken, NJ, USA, 2005), 3rd ed.

[70] D. Frickey, Conversions between S, Z, Y, H, ABCD, and T parameters which are valid for complex source and load impedances, IEEE Trans. Microw. Theory Tech. **42,** 205 (1994).